Mechanical Systems and Signal Processing 74 (2016) 183–198

Contents lists available at ScienceDirect

Mechanical Systems and Signal Processing

journal homepage: www.elsevier.com/locate/ymssp

Rotor anisotropy as a blade damage indicator for wind turbine structural health monitoring systems

Dmitri Tcherniak

Brüel & Kjær Sound & Vibration Measurement, Skodsborgvej 307, Nærum 2850, Denmark

ARTICLE INFO

Article history:
Received 10 October 2014
Received in revised form
13 July 2015
Accepted 27 September 2015
Available online 23 October 2015

Keywords:
Rotor anisotropy
Floquet analysis
Linear periodic time variant system
Wind turbine
Operational modal analysis

ABSTRACT

Structural damage of a rotor blade causes structural anisotropy of the rotor. In rotor dynamic, the anisotropy affects the symmetry of the rotor mode shapes, and the latter can be utilized to detect the blade damage. The mode shape symmetry can be characterized by relative blades' magnitude and phase. The study examines the potential use of these parameters as rotor damage indicators.

Firstly the indicators are studied analytically using a simple 6 degrees-of-freedom model of a rotating rotor. Floquet analysis is used due to the time periodic nature of the considered system. Floquet analysis allows one to perform analytical modal decomposition of the system and study the sensitivity of the damage indicators to the amount of damage. Secondly, operational modal analysis (OMA) is involved to extract the same damage indicators from simulated experimental data, which was synthesized via numerical simulations.

Finally, the same procedure was applied to operating Vestas V27 wind turbine, first using the simulated experimental data obtained by using aeroelastic simulation code HAWC2 and then using the data acquired during the measurement campaign on a real wind turbine.

The study demonstrates that the proposed damage indicators are significantly more sensitive than the commonly used changes in natural frequency, and in contrast to the latter, can also pinpoint the faulty blade. It is also demonstrated that these indicators can be derived from blades vibration data obtained from real life experiment.

1. Introduction

Blades of modern wind turbines are complex, high-tech structures, and their cost constitutes a significant part of the entire wind-turbine cost. While operating, the blades are heavily loaded and exposed to harsh weather conditions, especially for off-shore wind turbines. If damage to the blades develops to a critical level, it may cause catastrophic consequences. If the damage leads to partial or complete loss of structural integrity, repair is extremely costly, or may even be impossible. This calls for automatic blade health monitoring systems that are able to automatically detect and report damage, follow up on damage development and guide the blade Operational and Maintenance programme in general.

The damage detection approach presented in this paper generally follows the traditional concept: we extract modal parameters from the vibration data measured on an operating wind turbine; the potential changes in the modal parameters

E-mail address: dtcherniak@bksv.com

http://dx.doi.org/10.1016/j.ymssp.2015.09.038
0888-3270/

are used to detect and localize the damage [1]. Time-periodic nature of an operating wind turbine complicates modal analysis, and it is important to take this into consideration. This issue will be discussed later.

However, in this study, we take a pragmatic view: we are looking for the blade damage features sufficiently *sensitive*, and these features should be *observable* in a real-life situation. The following two examples demonstrate the opposite: It is known that damage changes natural frequencies of the structure. However, many conclude [2] that these changes are not sensitive to the damage; that is, the damage must grow to an extreme amount to change the natural frequencies significantly enough to be detectable. It is also known that the mode shapes of flapwise blade modes can be used to localize blade damage [3]. However, it was shown [4,5] that for operating wind turbines, the flapwise modes are not observable with the accuracy level sufficient for damage localization.

For modal parameter estimations, we use operational modal analysis (OMA) [6], which does not require the excitation force to be measured, and extracts modal parameters based on response data only, given that the structure is excited by ambient operational forces. We need to admit that OMA, though a valuable tool for big structures, is not perfectly suited for operating wind turbines. The acting aerodynamic loads do not satisfy OMA assumptions [7] and, in general, an operating wind turbine cannot be modelled as a time-invariant system. A linear time-periodic (LTP) system is a better model for an operating wind turbine; for modal decomposition of such systems, a number of dedicated methods have been developed, for example [8,9]. However, here we also take a pragmatic approach: the goal is not to perform a perfect modal identification, but rather be able to extract few modal-based dynamic features, which are sensitive to damage and which can be used for confident damage detection.

Floquet theory describes the complex dynamic of a rotating rotor via periodic modes: each mode can be presented via superposition of Fourier components oscillating at different frequencies. In theory, there is an infinite number of Fourier components even in a system with few degrees-of-freedom. Full modal analysis of a general time-periodic system is incredibly difficult. However, practical observations can pinpoint the dynamic features, which are sensitive to rotor anisotropy and can be identified from measured data and thus can serve the purpose of blade damage detection.

This explains the selection of damage features for this study: From practical experience [5], it was noticed that the magnitude and phases between the blades for *whirling modes* demonstrate a high level of sensitivity to blade damage. Also from experience [4,5], it is known that the *edgewise whirling* modes can be identified with a high level of confidence. Based on these observations, it was decided to examine how a slight rotor anisotropy due to blade damage influences the mode shape of the edgewise whirling modes, with the focus on phase and magnitude of the blade motion.

The rotor anisotropy also affects the tower; here we also propose and examine a damage indicator based on the changes in the tower dynamics.

The idea of using rotor anisotropy as a damage indicator was initially suggested in [10]; the present paper further develops the idea and exemplifies it by three means: (i) a simple lumped-mass model; (ii) simulated experiment using data generated by nonlinear aeroelastic code HAWC2 and (iii) by using experimental data obtained from an operating Vestas V27 wind turbine.

The paper applies the following investigation strategy: Section 2 sets up a lumped-mass model of a three-bladed rotor, simple but sufficient for catching the effects of rotor anisotropy for in-plane[1] rotor modes. The equations of motion are derived, and modal decomposition based on Floquet analysis is performed. Section 3 examines the differences in dynamics of isotropic and anisotropic rotors, and based on this, Section 4 suggests and studies the dynamic features that can be used as damage indicators. The sensitivity of these features to the amount of damage is examined.

In order to utilize the proposed damage indicators in practice, it should be possible to obtain the proposed damage indicators from measured data. Section 5 addresses the experimental techniques applicable to anisotropic rotors. The techniques are demonstrated on three cases with increasing complexity:

1. The first case (Section 5.1) is based on simulated data from a numerical experiment on the simple lumped-mass model introduced in Section 1.
2. The second case (Section 5.2) is based on numerical simulation of dynamics of operating Vestas V27 wind turbine. The simulations were conducted using non-linear aeroelastic code HAWC2.
3. The third case (Section 5.3) uses the blade vibration data recorded during a measured campaign on a real Vestas V27 wind turbine.

2. Simplified rotor model

A simple six degree-of-freedom (DOF) system (Fig. 1) models a rotating rotor and the supporting tower/nacelle structures. Each blade is modelled as two beams with lengths a and b, connected by a linear angular spring with stiffness k_l, $l=1$, …, 3, where l is the blade index. The blades are evenly distributed over the rotor, the blades' azimuth angles are:

[1] Due to blade pitch, the edgewise blade motion corresponds to in-plane rotor motion when the wind turbine is operating, and to out-of-plane when it is idle.

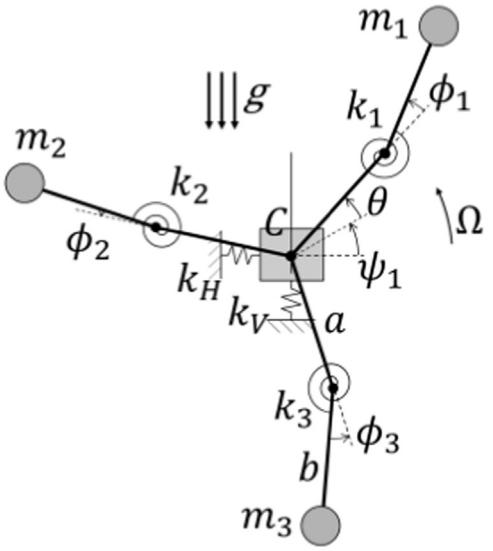

Fig. 1. Simplified rotor system.

$\psi_l(t)=\psi(t)+\frac{2\pi}{3}(l-1)$. Lumped masses m_l are attached to the ends of the outer beams. The rotor rotates with angular speed Ω about point C attached to the mass m_N; the latter models the nacelle. The mass is supported by two springs with stiffnesses k_H and k_V, which model the tower. The drivetrain has a moment of inertia I_D and stiffness k_D. A similar lumped parameter system is considered in [12]; however, there the focus was on the out-of-plane rotor motion.

2.1. Equation of motion and Coleman transformation

The system is described by six coordinates: x_C and y_C are the coordinates of point C, the deflection of each blade from a straight line is described by angle ϕ_l, and θ is the drivetrain angular vibrations.

Equations of motion (EoM) are derived using the Lagrange method. The linearized EoM can be written as

$$\mathbf{M}(t)\ddot{\mathbf{y}}(t)+\mathbf{G}(t)\dot{\mathbf{y}}(t)+\mathbf{K}(t)\mathbf{y}(t)=0, \tag{1}$$

where $\mathbf{M}(t)$, $\mathbf{G}(t)$ and $\mathbf{K}(t)$ are mass, gyroscopic and stiffness matrices. The matrices depend on the rotor azimuth $\psi(t)$; for constant rotor speed Ω, $\psi(t)=\Omega t$, the matrices are periodic with rotor period $T=2\pi/\Omega$: $\mathbf{M}(t)=\mathbf{M}(t+T)$, $\mathbf{G}(t)=\mathbf{G}(t+T)$, $\mathbf{K}(t)=\mathbf{K}(t+T)$. The vector $\mathbf{y}(t)=\{x_C(t),y_C(t),\phi_1(t),\phi_2(t),\phi_3(t),\theta(t)\}^T$ describes the physical DOFs of the system measured from the equilibrium position. Note the mixture of displacement and angular units in the vector.

The *Coleman* (also known as *multiblade coordinate* or *MBC*) *transformation* converts the blade DOFs $\phi_j(t)$ to multiblade coordinates [11]:

$$\begin{aligned} a_0(t)&=\frac{1}{3}\sum_{l=1}^{3}\phi_l(t)\\ a_1(t)&=\frac{2}{3}\sum_{l=1}^{3}\phi_l(t)\cos(\psi_l(t))\\ b_1(t)&=\frac{2}{3}\sum_{l=1}^{3}\phi_l(t)\sin(\psi_l(t)) \end{aligned} \tag{2}$$

The backward Coleman transformation converts the multiblade coordinates back to the blade coordinates:

$$\phi_l(t)=a_0(t)+a_1(t)\cos(\psi_l(t))+b_1\sin(\psi_l(t)). \tag{3}$$

In matrix form the transformation (3) can be written as

$$\mathbf{y}(t)=\mathbf{D}(t)\mathbf{w}(t), \tag{4}$$

where $\mathbf{w}(t)=\{x_C(t),y_C(t),a_0(t),a_1(t),b_1(t),\theta(t)\}^T$ is the vector of multiblade coordinates. The matrix $\mathbf{D}$ can be easily derived from (2) or found in, for example, [11]. It has the following properties [11]: $\mathbf{D}(t)^{-1}=\boldsymbol{\Gamma}\mathbf{D}(t)^T$, $\dot{\mathbf{D}}(t)=\mathbf{D}(t)\mathbf{R}$ and $\ddot{\mathbf{D}}(t)=\mathbf{D}(t)\mathbf{R}^2$. Knowing matrix $\mathbf{D}$, the matrices $\boldsymbol{\Gamma}$ and $\mathbf{R}$ can be easily derived, and it can be shown that they are time-invariant. Applying

the transformation to (1), using the above-mentioned properties and pre-multiplying by $\mathbf{D}(t)^{-1}$ yield the equation of motion in multiblade coordinates:

$$\mathbf{M}_D(t)\ddot{\mathbf{w}}(t)+(2\mathbf{M}_D(t)\mathbf{R}+\mathbf{G}_D(t))\dot{\mathbf{w}}(t)+\left(\mathbf{M}_D(t)\mathbf{R}^2+\mathbf{G}_D(t)\mathbf{R}+\mathbf{K}_D(t)\right)\mathbf{w}(t)=0, \tag{5}$$

where $\mathbf{M}_D(t)=\boldsymbol{\Gamma}\mathbf{D}(t)^T\mathbf{M}(t)\mathbf{D}(t)$, $\mathbf{G}_D(t)=\boldsymbol{\Gamma}\mathbf{D}(t)^T\mathbf{G}(t)\mathbf{D}(t)$ and $\mathbf{K}_D(t)=\boldsymbol{\Gamma}\mathbf{D}(t)^T\mathbf{K}(t)\mathbf{D}(t)$.

The important property of the Coleman transformation is that *for isotropic rotors*: $m_1=m_2=m_3=m$ and $k_1=k_2=k_3=k$, the mass and gyroscopic matrices are *time-invariant*: $\mathbf{M}_D(t)=\mathbf{M}_D$ and $\mathbf{G}_D(t)=\mathbf{G}_D$; the stiffness matrix is also time-invariant in the absence of gravity, $\mathbf{K}_D(t)=\mathbf{K}_D$. In the presence of gravity, the latter becomes time-periodic with period $T/3$. Thus, for isotropic rotors, if the influence of gravity is neglected, the Coleman transformation converts the time-periodic EoM (1) into the time-invariant one:

$$\mathbf{M}_D\ddot{\mathbf{w}}(t)+(2\mathbf{M}_D\mathbf{R}+\mathbf{G}_D)\dot{\mathbf{w}}(t)+\left(\mathbf{M}_D\mathbf{R}^2+\mathbf{G}_D\mathbf{R}+\mathbf{K}_D\right)\mathbf{w}(t)=0, \tag{6}$$

and thus allows application of eigenvalue analysis to EoM (6). Let the rth mode of (6) have the eigenvalue $\lambda_r=i\omega_r-\sigma_r$ and the mode shape $\mathbf{r}_r$, which is defined in multiblade coordinates: $\mathbf{r}_r=\{X_C,Y_C,A_0,A_1,B_1,\Theta\}_r^T$, $\mathbf{r}_r\in\mathbb{C}^{6\times1}$. The oscillations at this mode are $\mathbf{r}_re^{\lambda_rt}$. Using the backward Coleman transformation (3) and recalling the lth blade's azimuth $\psi_l(t)=\Omega t+\frac{2\pi}{3}(l-1)$, it is straightforward to convert the mode shape from the multiblade coordinates to the blade coordinates:

$$q_{l,r}(t)=A_{0,r}e^{i\omega_rt-\sigma_rt}+\tfrac{1}{2}\left(A_{1,r}-iB_{1,r}\right)e^{i(\omega_r-\Omega)t-\sigma_rt-i\frac{2\pi}{3}(l-1)}+\tfrac{1}{2}\left(A_{1,r}+iB_{1,r}\right)e^{i(\omega_r+\Omega)t-\sigma_rt+i\frac{2\pi}{3}(l-1)}. \tag{7}$$

Thus, in blade coordinates, the rth mode consists of three components. The first one oscillates at frequency ω_r, all the blades have the same magnitude and move in phase. This component is called *collective*. The second component is called *forward whirling*, it oscillates at $\omega_r-\Omega$, all blades have same magnitudes and the phase lag between the blades is the same for all blades and is equal to $\frac{2\pi}{3}$ (or 120°). The third, *backward whirling* component, oscillates at $\omega_r+\Omega$, and again all blades have same magnitudes and the phase lag between the blades is $-\frac{2\pi}{3}$ (or $-120°$).

The latter two components are called *whirling* because, when visualized, they resemble a whirl rotating in the rotor direction (*forward* whirling) and in opposite direction (*backward* whirling).

2.2. Floquet analysis

In this study, a deviation from the rotor isotropy is in focus, and the Coleman transformation followed by the eigenvalue analysis cannot be applied. Still, since the considered deviations from isotropy are assumed small, the results of the eigenvalue analysis of (5) might be useful as a starting point.

Let us consider the rotor becoming slightly anisotropic, for example due to damage that causes some reduction of the stiffness of one of the blades. In this situation, the EoM (5) will have time-periodic coefficient matrices. To obtain a solution to the time-periodic EoM, several techniques could be employed. Skjoldan, in his Ph.D. thesis, describes and compares several applicable methods (Table 3.1 in [14]); in this study, the classical Floquet analysis was chosen as the most appropriate.[2]

The first-order form of (1) is

$$\dot{\mathbf{x}}(t)=\sim\mathbf{A}(t)\mathbf{x}(t), \tag{8}$$

where $\mathbf{x}(t)=\left\{\dot{\mathbf{y}}(t)^T,\mathbf{y}(t)^T\right\}^T$ is the state vector (in multiblade coordinates) and $\sim\mathbf{A}(t)=\sim\mathbf{A}(t+T)$ is the periodic system matrix, the size of which is 12×12:

$$\sim\mathbf{A}(t)=\begin{pmatrix}-\mathbf{M}(t)^{-1}\mathbf{G}(t) & -\mathbf{M}(t)^{-1}\mathbf{K}(t)\\ \mathbf{I}_{6\times6} & 0_{6\times6}\end{pmatrix}. \tag{9}$$

Extending Coleman transformation to the first-order form:

$$\mathbf{x}(t)=\mathbf{B}(t)\mathbf{z}(t), \tag{10}$$

one arrives at the first-order equation in multiblade coordinates:

$$\dot{\mathbf{z}}(t)=\mathbf{A}(t)\mathbf{z}(t), \tag{11}$$

where $\mathbf{A}(t)=\sim\mathbf{A}(t)\mathbf{B}(t)$.

Following [15], the analysis is performed in a number of steps:

[2] With insignificant changes, this paper uses the notations and follows the derivation given in [15], where more details are provided.

1. The *fundamental matrix* of the system is built: Eq. (11) is numerically integrated for 12 linearly independent initial conditions. Denoting the solution for the jth initial condition at time t as $\boldsymbol{\varphi}_j(t)$, the fundamental matrix is written as

$$\boldsymbol{\Phi}(t) = \left[\boldsymbol{\varphi}_1(t) \quad \dots \quad \boldsymbol{\varphi}_{12}(t) \right]; \tag{12}$$

where $\boldsymbol{\Phi}(0) = \mathbf{I}$.
2. Then the *monodromy matrix* is computed as

$$\mathbf{C} = \boldsymbol{\Phi}(0)^{-1}\boldsymbol{\Phi}(T) = \boldsymbol{\Phi}(T); \tag{13}$$

3. As *Lyapunov–Floquet transformation* transforms the time-periodic system (11) into a time-invariant one, we can compute its system matrix $\mathbf{R}$ as

$$\mathbf{R} = \frac{1}{T}\ln(\mathbf{C}); \tag{14}$$

4. Eigenvalue decomposition of matrix $\mathbf{R}$ is performed:

$$\mathbf{R} = V\boldsymbol{\Lambda}\mathbf{V}^{-1}, \tag{15}$$

where the columns of $\mathbf{V}$ are the eigenvectors $\mathbf{v}_j$, and the diagonal elements of $\boldsymbol{\Lambda}$ are the eigenvalues $\lambda_j = \sigma_j + \mathrm{i}\omega_j$, the real part is the damping and the imaginary part is the frequency. Actually, the same eigenvalues can be obtained as

$$\lambda_j = \frac{\ln\left(\rho_j\right)}{T}, \tag{16}$$

where ρ_j are the eigenvalues of the monodromy matrix $\mathbf{C}$.
5. The *periodic mode shape* of the system (11) in the multiblade coordinates, is

$$\mathbf{r}_j(t) = \boldsymbol{\Phi}(t)\mathbf{v}_j e^{-\lambda_j t}, \tag{17}$$

6. In the blade coordinates, this is

$$\mathbf{u}_j(t) = \mathbf{B}(t)\mathbf{r}_j(t) = \mathbf{B}(t)\boldsymbol{\Phi}(t)\mathbf{v}_j e^{-\lambda_j t}. \tag{18}$$

7. Since the logarithm in (16) is complex, any $\lambda_j = \sigma_j + \mathrm{i}(\omega_j \pm n\Omega), n \in \mathbb{Z}$ are also eigenvalues of $\mathbf{R}$. Similar to the principal value of a complex logarithm, the principal frequency is defined as

$$\omega_{pj} = \omega_j - n_j\Omega, n_j{:}\omega_{pj} \in]-\Omega/2;\Omega/2] \tag{19}$$

and the principal eigenvalue as $\lambda_{pj} = \sigma_j + \mathrm{i}\omega_{pj}$. This is not a unique way to designate the principal eigenvalue. From practical considerations it is often more convenient to designate ω_{pj} closest to the corresponding natural frequency of the underlying LTI system, when $\Omega = 0$.
8. The jth periodic mode shape (17) computed for the principal eigenvalue λ_{pj} is expanded to the Fourier series, the most dominant Fourier component is identified, and its frequency is $n_{0j}\Omega$. For the isotropic rotor in the absence of gravity, the frequencies $\omega_{pj} + n_{0j}\Omega$ coincide with the eigenfrequencies of the time-invariant system (5).
9. Finally, the periodic mode shape in blade coordinates (18) is also expanded to the Fourier series. The dominating Fourier components will be concentrated around the frequency $\omega_{pj} + n_{0j}\Omega$. The behaviour of these components for different degrees of anisotropy are examined in the next section.

3. Examination of the modal dynamic

For examination of the rotor modal behaviour, the following parameters were chosen:

$m_N = 446{\bullet}10^3\mathrm{kg}$,

$m_1 = m_2 = m_3 = 41.7{\bullet}10^3\mathrm{kg}$,

$k_1 = k_2 = k_3 = 2.006{\bullet}10^8\mathrm{Nm}$,

$k_D = 10^8\mathrm{Nm}$,

$k_H = 2.610^6\mathrm{N/m}$,

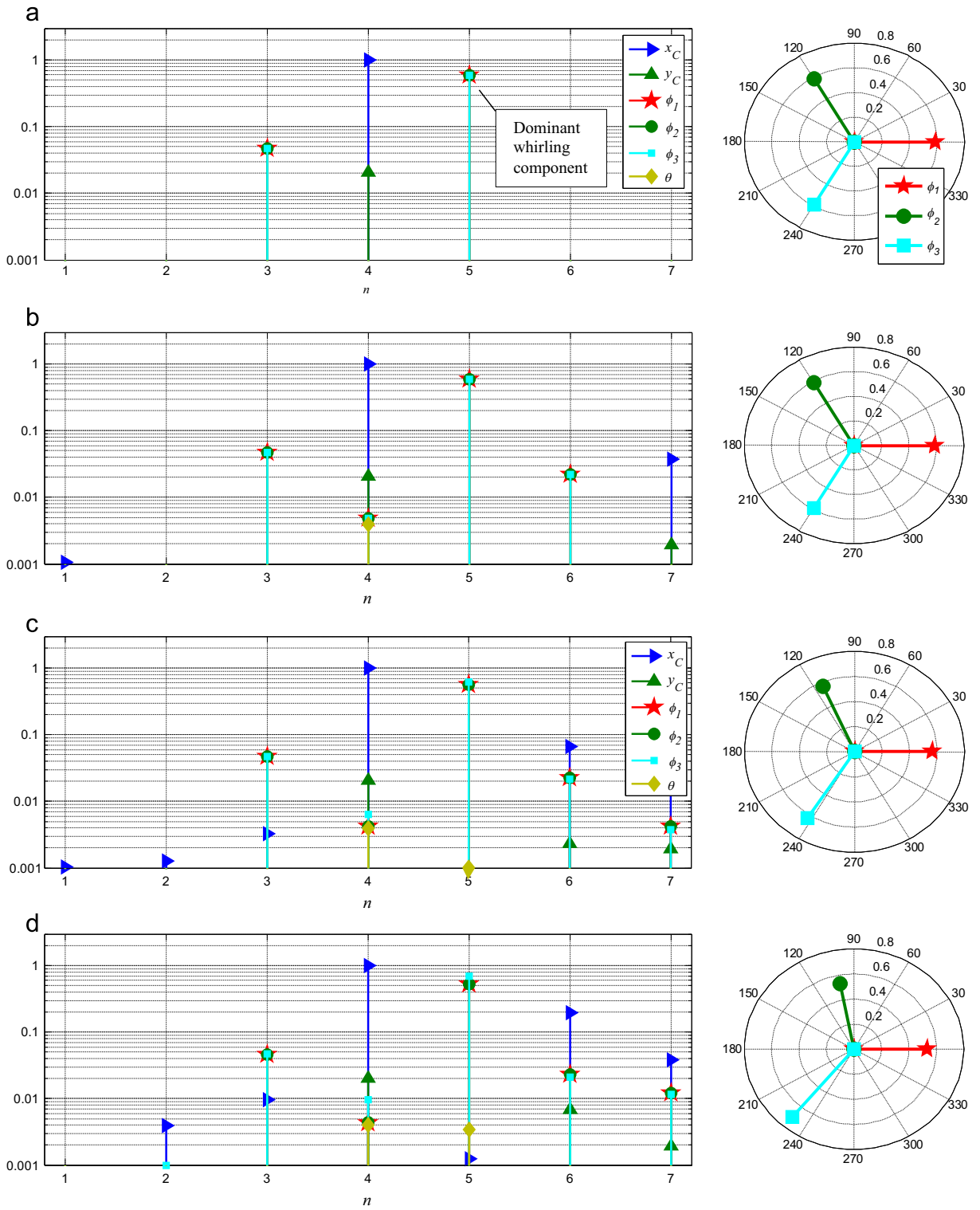

Fig. 2. Backward whirling mode. Left: magnitude of Fourier components; right: complexity plot of the dominant whirling component $n=5$: (a) isotropic rotor, no gravity; (b) isotropic rotor, with gravity; (c) anisotropic rotor, $k_c=0.99k$, with gravity; and (d) anisotropic rotor, $k_c=0.97k$, with gravity.

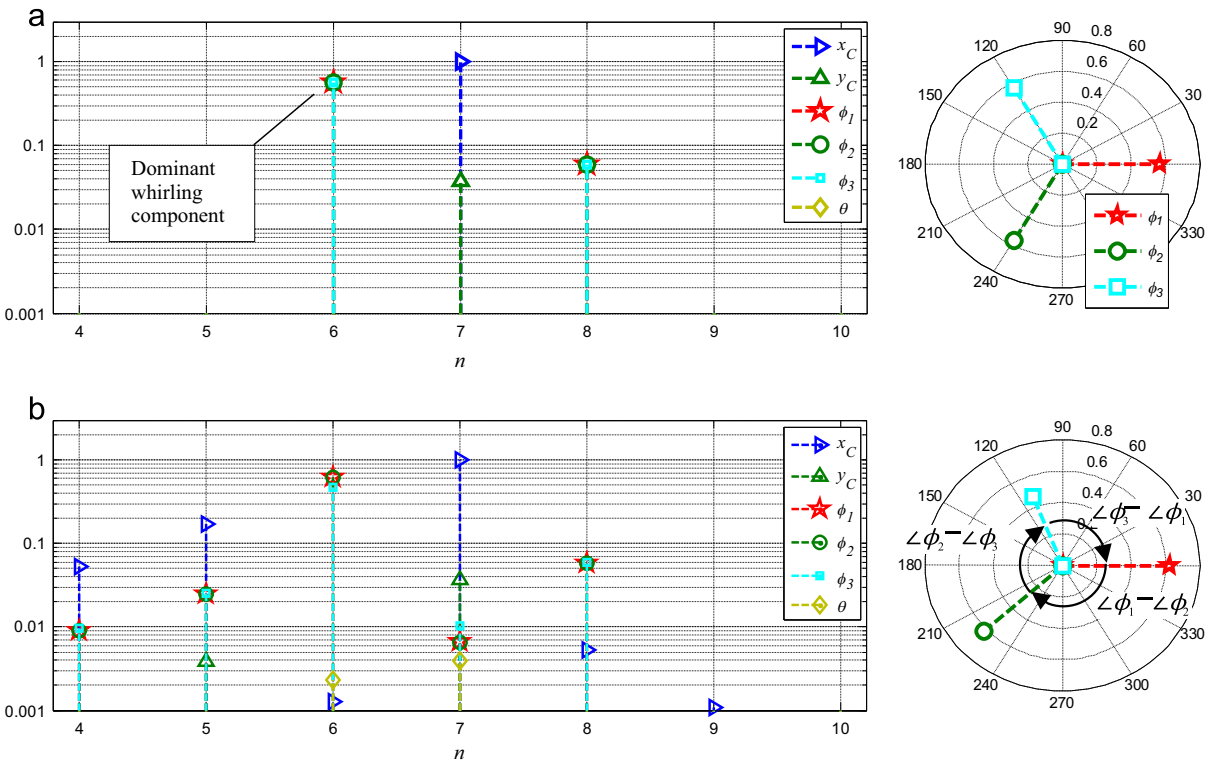

Fig. 3. Forward whirling mode. Left: magnitude of Fourier components; right: complexity plot of the dominant whirling component $n=6$: (a) isotropic rotor, no gravity and (b) anisotropic rotor, $k_3=0.97k$, with gravity.

$$k_V = 5.210^8 N/\mathrm{m},$$

$$I_D = 2.6{\bullet}10^7 \mathrm{kgm}^2,$$

$$a = b = 13.1m,$$

$$\Omega = 2\pi 0.16 \mathrm{rad/s}.$$

These parameters approximate the parameters of a generic 10 MW wind turbine model. A proportional damping term was introduced to (1): $(\alpha\mathbf{M}(t)+\beta\mathbf{K}(t))\dot{\mathbf{y}}(t)$; $\alpha=0.05, \beta=0.003$ were chosen for the examination.

Fig. 2a, c, e, and g show the amplitudes of the Fourier components of the *backward whirling* mode; its principal frequency is $\omega_{pBW} \approx$ Hz and $n_{0BW}=4$. The mode is normalized so that the dominant component amplitude is unity. When the rotor is isotropic, with no gravity (Fig. 2a), the mode consists of three components, (i) horizontal motion of the nacelle (x_C coordinate) at frequency $\omega_{pBW}+4\Omega \approx 0.716$ Hz, (ii) backward whirling at $\omega_{pBW}+5\Omega \approx 0.876$Hz and (iii) forward whirling at $\omega_{pBW}+3\Omega \approx 0.556$ Hz. The magnitude of the forward whirling component is one decade smaller than the backward whirling component, and it vanishes completely if the rotor support is symmetric, that is, $k_V=k_H$. The mode is called *backward whirling* since the rotor dynamic is dominated by the backward-whirling Fourier component.

Further in the text, we use the abbreviation BW for backward whirling and FW for forward whirling.

Complexity plot is a convenient tool for mode shapes visualization in the cases when the phase is neither 0° nor 180°. Fig. 2b shows the complexity plots of the dominating BW component ($n=5$). The phase lag between all three blades is the same, $-120°$, and the amplitudes of the blades are also exactly equal. As mentioned before, the same results could be obtained without Floquet analysis, by a much simpler Coleman transformation followed by eigenvalue decomposition of the system matrix **A** in (11), which is time-invariant in this case.

Due to gravity, this mode gets enriched by more Fourier components, but only two are significant: those at $\omega_{pBW}+6\Omega \approx 1.04$Hz and $\omega_{pBW}+7\Omega \approx 1.20$Hz (Fig. 2b). As observed from the complexity plot, the blade amplitudes are the same, as are the lags, $-120°$.

Let us introduce a slight rotor anisotropy by reducing the stiffness of the third blade: $k_3=0.99k$; these can be considered as a blade damage. Due to this, a horizontal motion appears at $\omega_{pBW}+6\Omega \approx 1.04$ Hz, but its magnitude is significantly smaller than the dominant horizontal motion ($n=4$). More interesting, one can see that the blades' phase lags start to

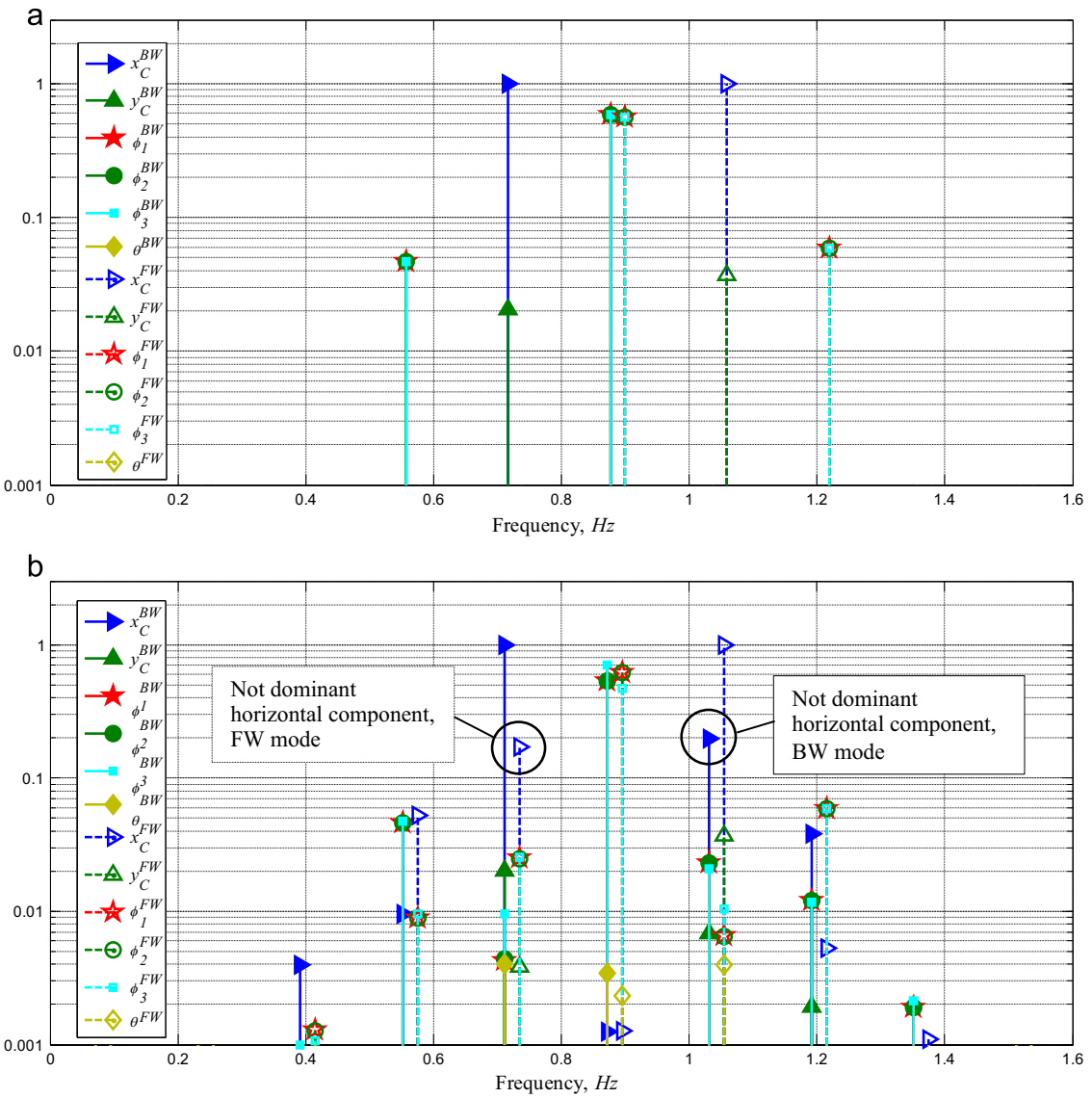

Fig. 4. Combined view of the BW and FW modes: (a) isotropic rotor, no gravity and (b) anisotropic rotor, $k_c=0.97k$, with gravity.

deviate from $-120°$: the lag between the undamaged blades 1 and 2 becomes less than 120°. In addition, the amplitudes of the different blades are not the same anymore (Fig. 2c): the amplitude of the damaged blade 3 is greater.

This behaviour becomes more pronounced when the stiffness k_3 decreases further (Fig. 2d).

Fig. 3 shows the Fourier components of the FW mode. For the isotropic rotor case, when no gravity is present, its principal frequency is $\omega_{\mathrm{pFW}} \approx -0.061$Hz and $n_{0FW}=7$. The mode is dominated by the horizontal motion of the nacelle at frequency $\omega_{pFW}+7\Omega \approx 1.06$Hz and FW at $\omega_{pFW}+6\Omega \approx 0.899$ Hz. The magnitude of the BW at $\omega_{pFW}+8\Omega \approx 1.22$Hz and the other components are significantly smaller. The mode is called *forward whirling* since the FW component dominates the rotor dynamics; the BW component is small and vanishes completely for the symmetric rotor support. The rotor anisotropy is clearly visible on the mode shape; however, the effect is opposite to what was observed on the BW mode. Here the amplitude of the weaker blade 3 is smaller compared to undamaged blades 1 and 2. The phase lag between the undamaged blades becomes greater than 120°, and grows with the increase of anisotropy. Also, the non-dominating horizontal component at $\omega_{pFW}+5\Omega \approx 0.739$ Hz appears and develops with the increase of anisotropy, though it is still a decade smaller that the dominant horizontal component.

One may notice that the frequency of the dominating whirling components of the two considered modes are very close: 0.876 Hz and 0.899 Hz. This is not just a coincidence. This phenomenon can be explained by the close natural frequencies of the vertical and horizontal rotor modes when the rotor does not rotate, see, for example, the Campbell diagram [13] (Fig. 2).

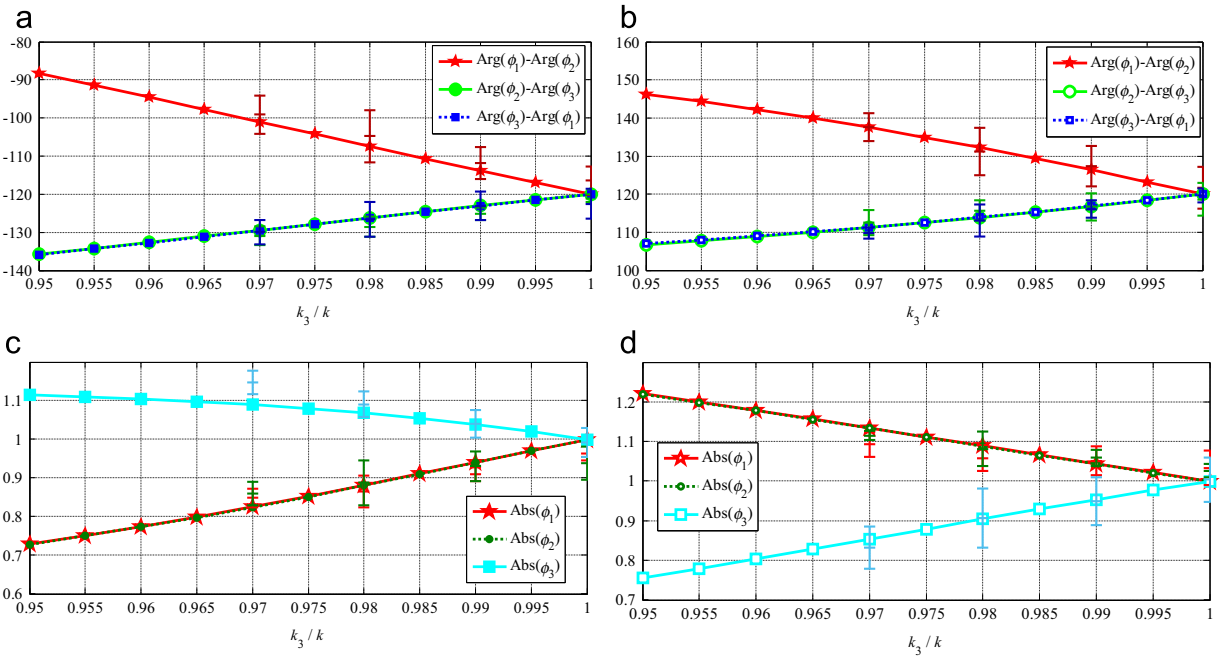

Fig. 5. Damage features vs. stiffness k_3: (a) phase lag BW mode; (b) same, FW mode; (c) normalized blades amplitudes, BW mode; and (d) same, FW mode.

If the vertical and horizontal stiffnesses of the supporting structure are equal, $k_V = k_H$, one should expect the frequencies of the dominating whirling components of the BW and FW modes to be exactly the same.

The proximity of the dominating whirling components of the two whirling modes, which is typical for operating wind turbines, creates a complex dynamic behaviour clearly observable on the measured spectra, as will be reported later in Sections 5.2 and 5.3. Fig. 4 illustrates this by combining the BW and FW modes on the same frequency axis, showing the case when both modes have the same magnitude.

4. Damage indicators

Based on the observations above, several modal-related damage indicators are proposed: (i) phase between the blades for the dominating whirling component; (ii) blade amplitudes of the dominating whirling component; and (iii) amplitude of the non-dominant horizontal component. The sensitivity of these damage indicators to the amount of damage is examined below.

The dominating whirling components are $n=5$ for BW mode and $n=6$ for FW mode (see Figs. 2 and 3). Fig. 5a and b show how the phase lag depends on k_3 for BW and FW respectively. The calculation of the phase lag is shown in Fig. 3b, right. One per cent reduction of k_3 causes the change of the phase lag between two undamaged blades by about 5–6% and 2–3% between damaged and undamaged blades.

All three blades have the same magnitude for isotropic rotors, but start to differ when the rotor becomes anisotropic, see Fig. 5c and d for BW and FW modes respectively. The damaged blade amplitude increases for the BW mode and decreases for the FW mode. The changes are about 4–6% for 1% reduction of k_3.

It is important to note that both features also indicate *which* blade is damaged.

The non-dominant horizontal component also increases with rotor anisotropy development. This is the Fourier component $n=6$ for the BW mode and $n=5$ for the FW mode (Figs. 2 and 3); it increases by about 5–7% per 1% reduction of k_3.

Considering use of this phenomenon as a damage indicator, the advantage is that it can be extracted from the nacelle acceleration measurements and does not require getting measurements from the blades, which is more difficult from the practical point of view. There are two drawbacks, however. This damage feature does not indicate which blade is damaged. Also, examining the spectra overview (Fig. 4), one can note that the non-dominant component of the FW mode is very close in frequency to the dominating component of the BW mode, and vice versa. This means that it might be difficult to extract this feature from bare spectra examination, and more advanced signal analysis techniques such as singular value decomposition (SVD) might be necessary.

For comparison, a one per cent decrease of k_3 causes only 0.14–0.17% change of the natural frequencies. Therefore, this damage indicator, which is typical in many SHM systems, is more than 30 times less sensitive to damage than those proposed in this study.

5. Experimental techniques

The analytical study in the previous section utilizes a possibility to integrate the known EoM. The objective of this section is to demonstrate that the suggested damage features are derivable from experimental data, when the EoM are unknown.

There are only a few methods capable of addressing LPTV systems from the experimental view point. For example, the above-mentioned Coleman transformation was suggested as a pre-processing step to OMA [16]. Following this approach, the experimentally obtained blade coordinates are converted to multiblade coordinates in the time domain, using (2). Then OMA provides modal parameters, with the mode shapes expressed in multiblade coordinates. Backward Coleman transformation (3) converts each mode shape into three Fourier components, each oscillating at the frequencies separated by Ω. As mentioned before, the method assumes an isotropic rotor. Attempts to apply it to an anisotropic rotor may lead to erroneous results, as was shown in [17]. In the context of this study, this method is not applicable at all: indeed, Eq. (7) shows that the shapes of the three components *always* have the same magnitudes for all blades, and the phase between the blades is *always* 0 or $\pm 120^\circ$. This means that the damage features suggested in Section 4 cannot be extracted using the Coleman transformation.

Another method suggested in [18] deals with the system's periodicity by sampling its state once per revolution, when the rotor is at exactly the same position. The drawback of this method is that it requires as many rotor revolutions as samples. In order to provide sufficient accuracy of the followed stochastic subspace identification, the observation period requires several thousand revolutions under stationary operating conditions. This is difficult to achieve in the case of wind turbines, where the wind conditions and rotor speed constantly change [19]. This method is more suitable for rapidly rotating rotors, for example helicopters rotors.

Another recently suggested method is based on the harmonic power spectra (HPS) suggested in [20], which was extended to the time domain [21] and dubbed H-OMA-TD. The core of the method is the exponential harmonic modulation of the measured response signals $\mathbf{y}(t)$:

$$\mathbf{y}_m(t) = \mathbf{y}(t)e^{-im\Omega}, \quad m = -M, \ldots, M \tag{20}$$

where Ω is the rotational speed and M is a small integer. After some treatment, the obtained time histories $\mathbf{y}_m(t)$ become the input to an OMA algorithm. This approach does not require the rotor and measurement system to be isotropic and outputs $2M+1$ correctly scaled Fourier components of the identified modes.

It is important to recall that the objective of this section is not to provide correct dynamic identification of the rotor but to extract the damage features proposed in Section 4. Here we suggest to apply OMA *directly* to the raw data measured on the rotor. This is incorrect from the modal identification point of view since the important content of the periodic modes, namely the linkage and correct scaling of the Fourier components, are being lost. Instead, the algorithm outputs the Fourier components as separate normalized modes. This is the same as setting $M=0$ in (20). However, from the damage features extraction point of view, this is sufficient. Indeed, according to Section 4, one needs to extract and monitor only *one* dominant whirling component of two modes, and this can be done by direct application of an OMA algorithm to the raw data.

In the following, the proposed experimental approach is demonstrated on three examples: (i) simulated behaviour of the 6DOF system on Fig. 1 excited by random uncorrelated noise, (ii) simulated vibrations of a Vestas V27 wind turbine due to modelled aeroelastic forces, and (iii) experimentally obtained vibration data from a real Vestas V27 wind turbine.

5.1. Application to the 6-DOF simplified rotor system

Here we model a measurement system installed on the simplified rotor (Fig. 1): accelerometers are attached to the tips of all blades, measuring in the tangential direction; two more accelerometers measure vertical and horizontal motion of the nacelle and an angular vibration accelerometer is installed on the drivetrain. All DOFs are excited by random, uncorrelated broadband noise. This excitation satisfies OMA assumptions, but we acknowledge that the real aeroelastic forces are different [7]. Then the EoM is numerically integrated using MATLAB's *ode45* routine, and the response time histories for the physical DOFs are obtained and converted to the signals that would be measured if the accelerometers were installed as described above. From now on, we assume that the excitation forces and the EoM are not known, and the damage features shall be derived from the observed responses only.

Time histories 7200 s long, which correspond to 1152 rotor revolutions, were synthesized and sampled at 50 Hz. The time histories were used as input to Brüel & Kjær Type 7760 OMA software. The modal analysis was performed using the Stochastic Subspace Iteration (SSI/UPC) algorithm. Four system states, one undamaged and three damaged ($k_3=0.99$, 0.98 and 0.97) were analysed. To collect statistics, five different load realizations were generated for each state. Thus, in total 20 analyses were performed.

The results of the simulated experiment are shown as error bars in Fig. 5. The centre tick denotes the mean of the five OMA runs, the upper and lower ticks denote 95% confidence interval. The damage features derived from the OMA results are in agreement with analytical values – there is significant dispersion, especially for the magnitudes, but the general tendency and the curve's slope are correctly reflected.

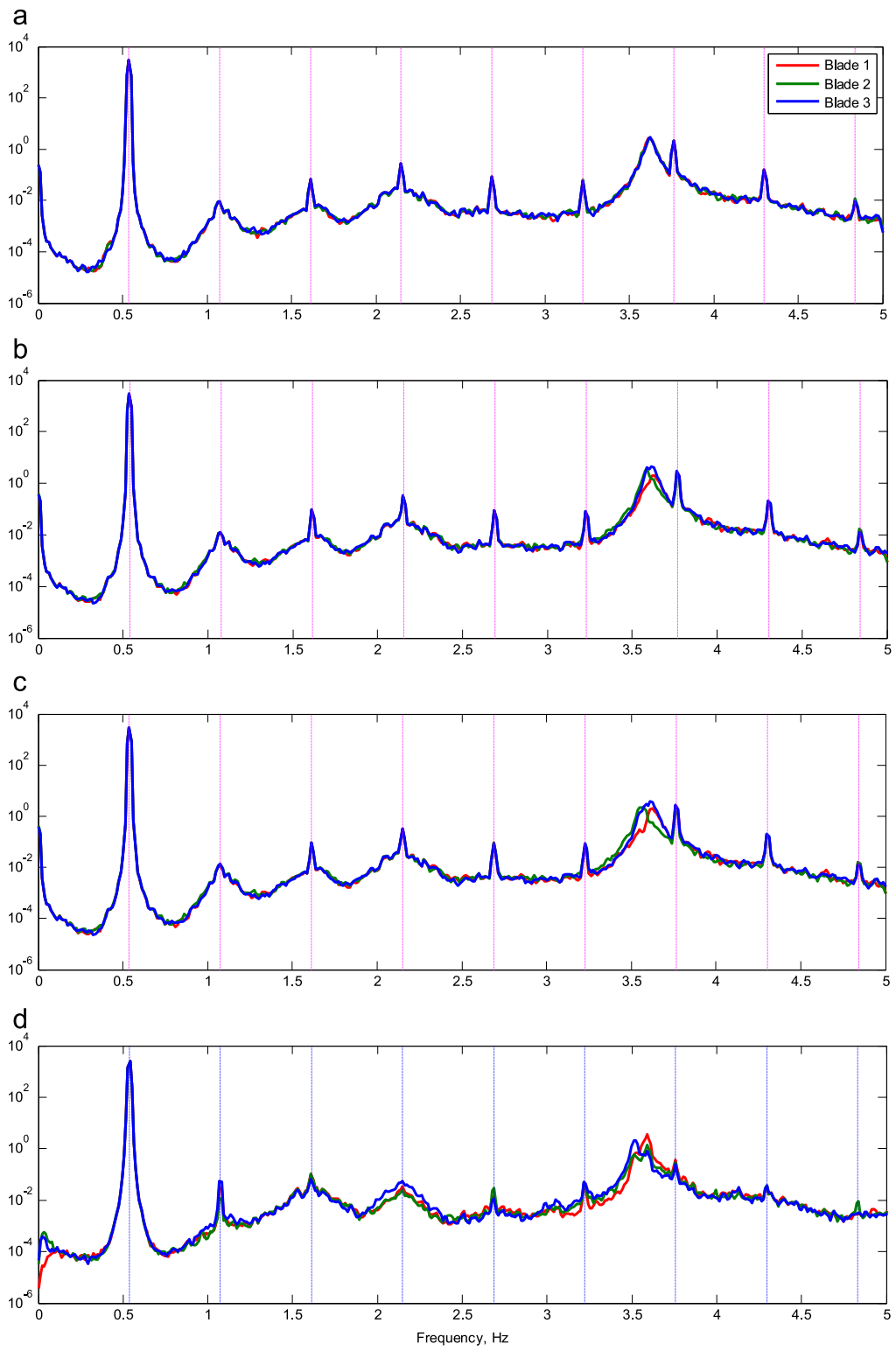

Fig. 6. Power spectral density of the three edgewise blade-tip accelerometers for low-speed regime (32 rpm): (a) HAWC2 simulation, isotropic rotor; (b) same, 3% Young modulus reduction of blade 2; (c) same, 5% Young modulus reduction of blade 2; and (d) experimentally obtained. The dotted lines indicate rotor harmonics.

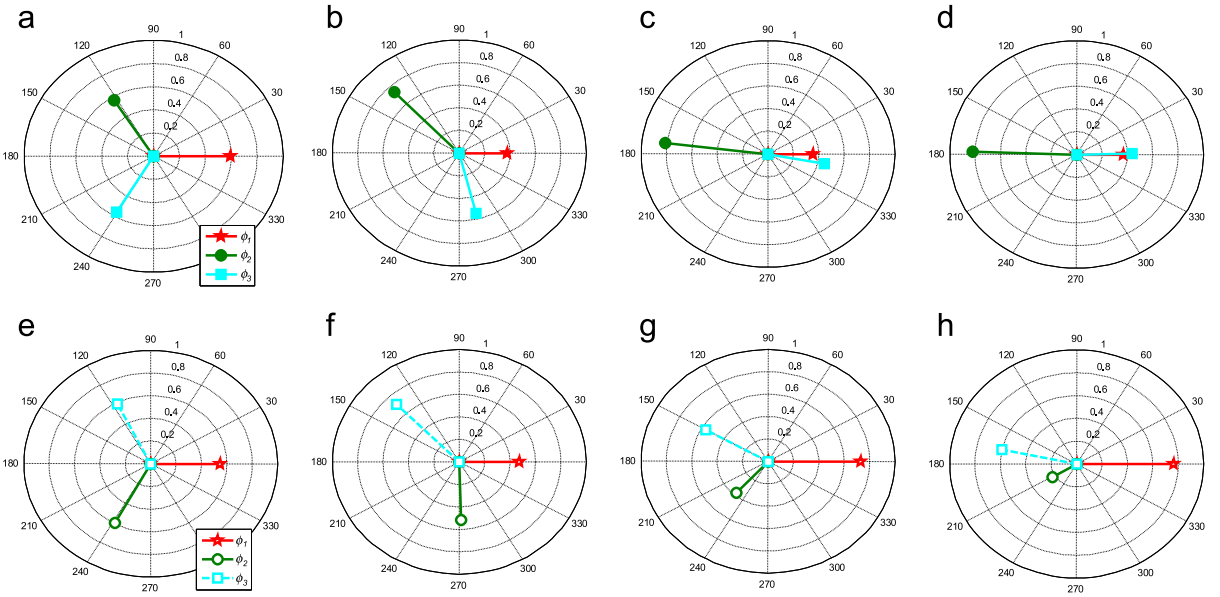

Fig. 7. Complexity plots of the dominant components of the whirling modes. Top: BW mode: (a) isotropic rotor; (b) 1% Young modulus reduction of blade 2; (c) 3% Young modulus reduction of blade 2; and (d) 5% Young modulus reduction of blade 2. Bottom: FW mode: (e) isotropic rotor; (f) 1% Young modulus reduction of blade 2; (g) 3% Young modulus reduction of blade 2; and (h) 5% Young modulus reduction of blade 2.

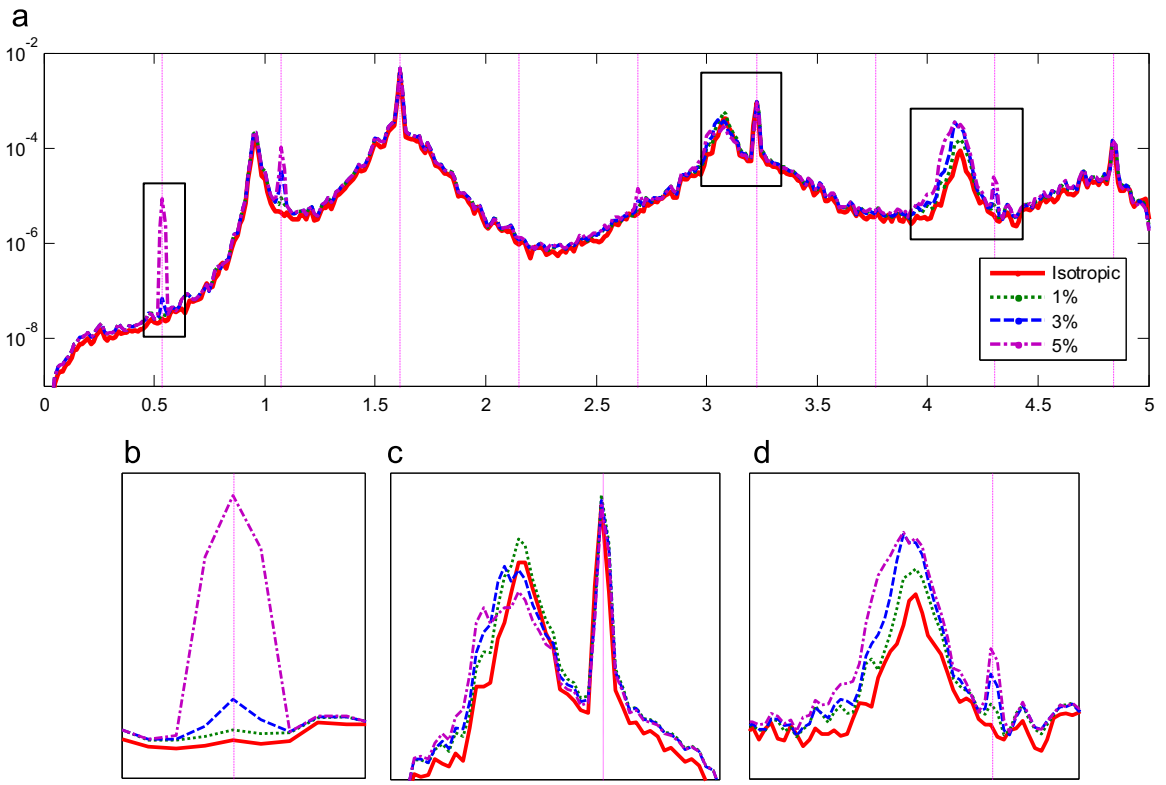

Fig. 8. Spectra of the simulated nacelle signal in side-to-side direction for different degree of anisotropy: (a) Overview; (b)–(d) insets corresponding to the boxes on the overview.

5.2. Application to simulated Vestas V27 wind turbine

As mentioned in the previous section, the aerodynamic loads acting on the rotor of an operating wind turbine are much more complicated than the uncorrelated broadband white noise used in the previous section. This section employs a more realistic load scenario by using a dedicated tool for simulation of operating wind turbine dynamics, HAWC2.

Horizontal Axis Wind turbine Code 2nd generation (HAWC2) is a nonlinear aeroelastic code designed for simulation of the wind turbine dynamic response in the time domain. It was developed and maintained by DTU Wind Energy department

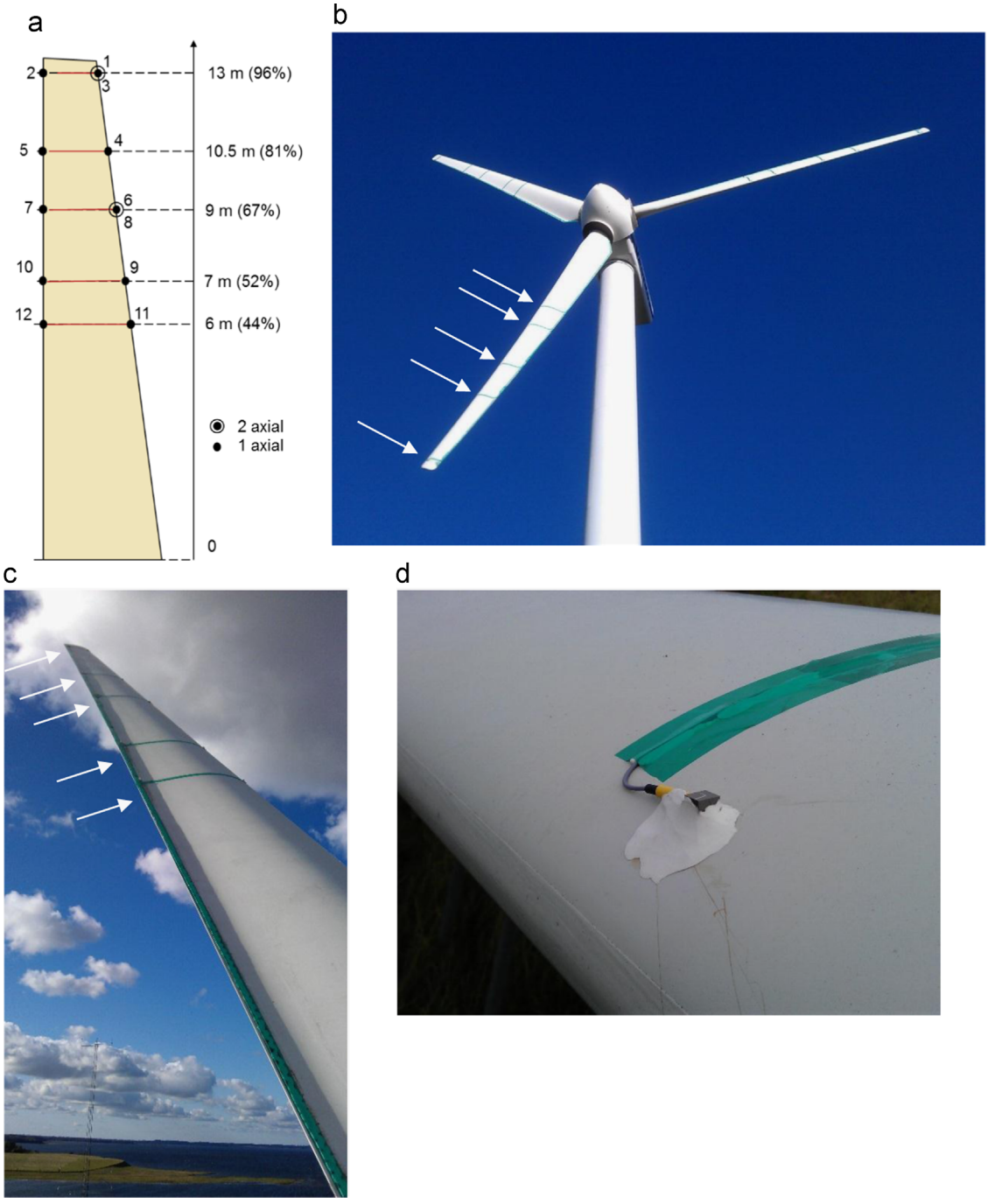

Fig. 9. Instrumentation of Vestas V27 wind turbine: (a) accelerometers placement on a blade. Dot – flapwise, circle – edgewise accelerometer; (b), (c) accelerometers on the leading and trailing edges of the blades, white arrows indicate accelerometer placement; (d) B&K Type 4507B6 mounted on a leading edge of one of the blades.

(formerly Risø Danish National Lab for Sustainable Energy). The structural part of the wind turbine is modelled by employing a multibody formulation, where each body is an assembly of Timoshenko beam elements. The aerodynamic part of the code is based on the blade element momentum (BEM) theory, extended to handle dynamic inflow. The gravity, wind shear and turbulence, as well as the wind turbine control system are modelled as well, making HAWC2 a powerful tool for the investigation of wind turbine dynamics; full control of the model and operational environments allows one to play "what–if" scenarios. More details about HAWC2 can be found in [22].

A Vestas V27 wind turbine was chosen as a test object. The main reason for the choice was that the experimental data for this wind turbine were available. On today's scale, the V27 is a relatively small wind turbine with 225 kW rated power, 27 m rotor diameter and the hub about 30 m above the ground. However, the V27 design is similar to modern horizontal-axis wind turbines; it is pitch-regulated and has three blades. The blades are relatively stiff, and the small rotor diameter determines the high rotor speed: the low-speed regime is 32 rpm and the high-speed regime is 43 rpm.

The HAWC2 model of the V27 was tuned to match the experimentally observed dynamics of the real V27 in both high- and low-speed regimes, under the observed wind conditions (taking into account the wind speed, shear and turbulence). The details of the model tuning can be found in [23]. Using the model, 20-min time histories were simulated (100 Hz sampling frequency, 120,000 samples) for isotropic and anisotropic rotors. The averaged spectra of the edgewise tip accelerometer signals for different degrees of rotor anisotropy are shown in Fig. 6a–c.

A structural anisotropy was introduced by reduction of Young modulus and shear stiffness of all elements constituting one blade, while the two other blades were kept unchanged. The anisotropy does not affect most of the simulated spectra; the only noticeable effect appears at the peaks around 3.6 Hz (Fig. 6a–c). As is known from the previous study [17], these peaks are due to the dominant whirling components of the first edgewise whirling modes, that is, those suggested as damage indicators in Section 4.

To quantify the phenomena, we extract the Fourier components using OMA. We used HAWC2 to simulated acceleration time histories at the tip point and the point located at 67% of the blade length, in edgewise direction, for all three blades. The time histories were input to OMA SSI/UPC and the dominating whirling components of the FW and BW modes were identified. As explained before, OMA outputs the Fourier components as normalized modes. Though the components are very close in frequency, it is not difficult to identify them and the find components' shapes. The complexity plots allow examination of the blades' magnitude and phase for each component shape (Fig. 7). The isotropic rotor features approximately equal magnitudes and the phase lag between the blades (Fig. 7a and d). Introduction of the anisotropy fundamentally changes the shape of both Fourier components: for the BW mode, the amplitude of Blade 2 grows relative to the magnitudes of the two other blades, and the phase lag between blades 1 and 3 gets smaller, approaching zero (Fig. 7d). For the FW mode, the magnitude of Blade 2 becomes smaller and the phase lag between Blade 1 and Blade 3 increases, approaching 180° (Fig. 7h). This readily identifies the blade with reduced Young modulus, namely Blade 2. These results qualitatively resemble the analytical results reported in Section 3 and illustrated by Figs. 2 and 3.

To illustrate the third damage indicator proposed in Section 4, the spectra of the tower top vibrations in a side-to-side direction are plotted in Fig. 8. The changes of the two peaks, around 3.1 Hz and 4.2 Hz are in focus; they are shown in insets of Fig. 8c and d respectively. For the isotropic rotor, these peaks correspond to the dominant horizontal components: the left to BW mode, and the right to FW mode, compare to Fig. 4a. When the rotor becomes anisotropic, the non-dominant horizontal components of the whirling modes appear (Fig. 4) and significantly change the magnitude and shape of the peaks (Fig. 8c and d).

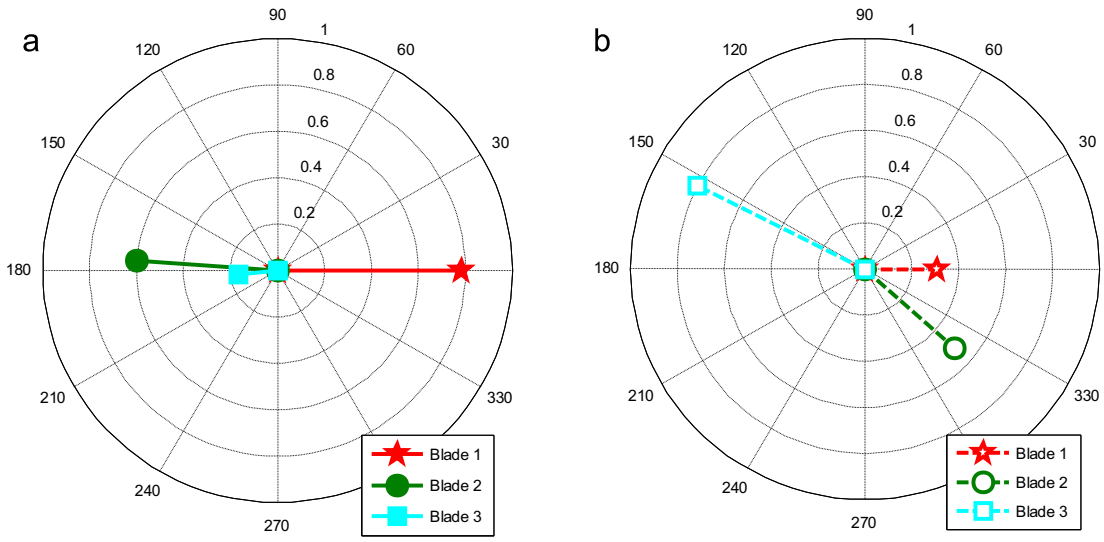

Fig. 10. Complexity plots of the dominant components of the whirling modes, obtained from experimental data: (a) BW mode and (b) FW mode.

An isotropic rotor has pronounced sharp peaks at 3p (blade pass frequency) and its harmonics. Structural anisotropy leads to rotor unbalancing, which shows itself as sharp peaks at 1p, 2p and some other harmonics. One can correctly suggest that the development of sharp peaks at these harmonics can act as a damage indicator. However, from the spectra in Fig. 8 (and inset Fig. 8a), one can hardly detect the peak at 1p for a slightly anisotropic rotor (1% stiffness reduction); in contrast, the peaks due to the whirling modes change noticeably even for a small amount of anisotropy (Fig. 8c and d). Difference in the blade masses (for example, due to ice formation on one of the blades) can be another reason of rotor unbalancing, causing similar effects on the spectra; the unbalancing due to mass anisotropy is not examined in the presented study.

Obviously, the magnitude and shape of the peaks of the tower response spectra are not a robust indicator for the rotor damage. A better technique might involve modal analysis to follow up the development of the non-dominant horizontal component of the whirling modes, which requires more sophisticated analysis tools. In practice, this could be done after damage has been detected by simpler methods. The thoughtful investigation of damage indicators based on tower acceleration signals is outside the scope of this study.

5.3. Application to experimental data from a Vestas V27 wind turbine

The results of this section are based on experimental data obtained during the measurement campaign, which took place from October 2012 through May 2013. The test wind turbine, a Vestas V27, which is a part of DTU Wind Energy test facilities, is located near Roskilde, Denmark (Fig. 9). Each blade of the V27 was instrumented with 12 accelerometers (Brüel & Kjær Types 4507 and 4508): 10 accelerometers in the flapwise direction, five on the leading edge and five on the trailing edge; and 2 accelerometers in the edgewise direction, one at the tip, and another at 67% of the blade length. Special care was taken to mount the sensors on all three blades as similar to each other as possible, both location- and direction-wise. The nacelle was instrumented with three triaxial accelerometers. The data streams from the rotor and nacelle were synchronized using IRIG-B signals. In addition to the sensors measuring structural vibration, more instruments were installed to provide the instantaneous rotor azimuth, rotor angular speed and blade pitch angle. In total, 40 channels were measured on the rotating part of the wind turbine using Brüel & Kjær LAN-XI data acquisition modules located in the hub and wirelessly transferred to the nacelle, where another 11 channels were measured. All channels were recorded at a sampling frequency of 4096 Hz. More details regarding the measurement setup can be found in [24]. Simultaneously, weather conditions such as wind speed, turbulence, wind direction, etc. were logged.

For the analysis, a 20-min dataset was selected that features a minimal pitch activity and rotor rpm variation. The power spectral density of the edgewise tip accelerometers averaged over the observation time are shown in Fig. 6d (for comparison with HAWC2 simulations, Fig. 6a–c.). Two edgewise accelerometer signals from each blade (in total 6 signals) were used as input to OMA. An identical modal identification procedure as for simulated time histories (Section 5.2) was used. Using OMA-SSI/UPC, two whirling components constituting the peak at 3.5–3.6 Hz where extracted, and their shapes were examined using complexity plots (Fig. 10).

Comparing with the simulated examples, one can observe a similar pattern in the complexity plots: for the BW mode, Blade 1 has the biggest magnitude, while the phase lag between Blade 2 and 3 is almost zero. For the FW mode, Blade 1 has the smallest magnitude, and the phase lag between Blades 2 and 3 is almost 180^0. Thus, one can suspect that Blade 1 has reduced structural stiffness compared to the other two blades. Of course, this is still a hypothesis; there could be other reasons for rotor anisotropy, for example mass unbalance, aerodynamic anisotropy due to pitch mismatch or some other reasons. Testing these hypotheses is out of scope of the present study.

6. Conclusion

Novel damage indicators for a potential SHM system of a wind turbine rotor are suggested and examined. The indicators are modal-based and utilize mode shape asymmetry due to rotor anisotropy caused by blade damage. It is demonstrated that these features are significantly more sensitive to the damage compared to the natural frequencies of the rotor. Moreover, the indicators can pinpoint which of the blades are different from the others. It is also shown that it is possible to extract these indicators from measured vibrations.

Employing a simple six DOF analytical model of a rotating rotor and using Floquet analysis, the exact modal decomposition was performed for isotropic and anisotropic rotors. Comparing the results, the dynamic features most affected by the anisotropy were found.

A simulated experiment using aeroelastic code HAWC2 confirmed that the damage features can be extracted from measured vibration responses using OMA.

The applicability of the proposed damage indicators to realistic data was confirmed using simulated and experimental data. Using wind turbine aeroelastic code HAWC2, it was possible to conduct a simulated experiment on a Vestas V27 wind turbine rotor with an increasing amount of damage and show that the damage indicators can correctly detect the damage and identify the damaged blade. Then the damage detection algorithm was applied to experimentally obtained data from a real Vestas V27, and a hypothesis of the cause of the observed rotor anisotropy was proposed.

In this paper, the use of the non-dominant horizontal component as a damage indicator was mentioned but not elaborated. This could be suggested as an interesting topic for the future research.

Acknowledgements

The work is partly supported by EUDP (Danish Energy Technology Development and Demonstration Programme), Grant no. 64011-0084 “Predictive Structure Health monitoring of Wind Turbines”. The author wishes to acknowledge the great help from Óscar Ramírez Requesón who performed the simulations of the Vestas V27 wind turbine.

References

[1] D. Montalvão, N.M.M. Maia, A.M.R. Ribeiro, A review of vibration-based structural health monitoring with special emphasis on composite materials, Shock Vib. Dig. 38 (4) (2006) 295–324.
[2] W. Fan, P. Qiao, Vibration-based damage identification methods: a review and comparative study, Struct. Health Monit. 10 (1) (2010) 83–111.
[3] M.D. Ulriksen, D. Tcherniak, P.H. Kirkegaard, L. Damkilde, Operational modal analysis and wavelet transformation for damage identification in wind turbine blades, In: Proceedings of 7th European Workshop on Structural Health Monitoring. Nantes, France, 2014.
[4] D. Tcherniak, J. Basurko, O. Salgado, I. Urresti, S. Chauhan, C.E. Carcangiu, M. Rossetti, Application of OMA to operational wind turbine, In: Proceedings of International Operational Modal Analysis Conference, Istanbul, Turkey, 2011.
[5] S. Yang, D. Tcherniak, M.S. Allen. Modal analysis of rotating wind turbine using multiblade coordinate transformation and harmonic power spectrum, In: Proceedings of 32nd International Modal Analysis Conference, Orlando, FL, USA, 2014.
[6] G. H. James, T. G. Carne Damping measurements on operating wind turbines using the natural excitation technique (NExT), In: Proceedings of 11th ASME Wind Energy Symposium presented at the Energy Sources Technology Conference and Exhibition, vol. 12, 1992, pp. 75–81.
[7] D. Tcherniak, S. Chauhan, M. H. Hansen, Applicability limits of operational modal analysis to operational wind turbines, In: Proceedings of 28th International Modal Analysis Conference, Jacksonville, FL, USA, 2010.
[8] M.S. Allen, M.W. Sracic, S. Chauhan, M.H. Hansen, Output-only modal analysis of linear time periodic systems with application to wind turbine simulation data, Mech. Syst. Signal Process. 25 (2011) 1174–1191.
[9] P.F. Skjoldan, M.H. Hansen, On the similarity of the Coleman and Lyapunov–Floquet transformations for modal analysis of bladed rotor structures, J. Sound Vib. 327 (2009) 424–439.
[10] D. Tcherniak, Loss of rotor isotropy as a blade damage indicator for wind turbine structural health monitoring system, In: Proceedings of 7th European Workshop on Structural Health Monitoring, Nantes, France, 2014, pp. 780–787.
[11] M.H. Hansen, Improved modal dynamics of wind turbines to avoid stall-induced vibrations, Wind Energy 6 (2003) 179–195.
[12] P.F. Skjoldan, O.A. Bauchau, Determination of modal parameters in complex nonlinear systems, J. Comput. Nonlinear Dyn. 6 (3) .
[13] M.H. Hansen, Aeroelastic instability problems for wind turbines, Wind Energy 10 (2007) 551–577.
[14] P.F. Skjoldan, Aeroelastic Modal Dynamics of Wind Turbines Including Anisotropic Effects (Ph.D. Dissertation), Risø, Denmark, 2011.
[15] P.F. Skjoldan. Modal dynamics of wind turbines with anisotropic effects, In: Proceedings of 47th AIAA Aerospace Sciences Meeting, Orlando, FL, USA, 2009.
[16] D. Tcherniak, S. Chauhan, M. Rossetti, I. Font, J. Basurko, O. Salgado, Output-only modal analysis on operating wind turbines: application to simulated data, In: Proceedings of European Wind Energy Conference, Warsaw, Poland, 2010.
[17] S. Yang, D. Tcherniak, M. S. Allen, Modal analysis of rotating wind turbine using multi-blade coordinate transformation and harmonic power spectrum, In: Proceedings of 32nd International Modal Analysis Conference, Orlando, FL, USA, 2014.
[18] A. Jhinaoui, L. Mevel, J. Morlier, A new SSI algorithm for LPTV systems: application to a hinged-bladed helicopter, Mech. Syst. Signal Process. 42 (1) (2014) 152–166.
[19] L. Mevel, I. Gueguen, D. Tcherniak, LPTV subspace analysis of wind turbine data, In: Proceedings of 7th European Workshop on Structural Health Monitoring, Nantes, France, 2014, pp. 221–228.
[20] M.S. Allen, Frequency-domain identification of linear time-periodic systems using LTI techniques, J. Comput. Nonlinear Dyn. 4 (4) (2009) 041004.
[21] D. Tcherniak, M. Allen, S. Yang. Experimental characterization of operating wind turbine using Harmonic Power Spectra and Stochastic Subspace Identification, In: Proceedings of Conference on Noise and Vibration Engineering (ISMA), Leuven, Belgium, 2014.
[22] T.J. Larsen, A.M. Hansen, How 2 HAWC2, the User's Manual, Ris-R-1597 (version 4-4) (EN), 2013.
[23] O. Ramirez, Identification of Modal Parameters Applying Operational Modal Analysis on a Full Scale Operating Vestas V27 Wind Turbine, DTU Wind Energy, 2014 (M.Sc. thesis).
[24] D. Tcherniak, G. C. Larsen, Applications of OMA to an operating wind turbine: now including vibration data from the blades, In: Proceedings of 5th International Operational Modal Analysis Conference, Guimarães, Portugal, 2013.